JOURNAL OF PROPULSION AND POWER
Vol. 25, No. 1, January–February 2009

Deep Space 1 Flight Spare Ion Thruster 30,000-Hour Life Test

Anita Sengupta,* John A. Anderson,† Charles Garner,† and John R. Brophy‡
Jet Propulsion Laboratory, California Institute of Technology, Pasadena, California 91109
Kim K. de Groh§ and Bruce A. Banks¶
NASA John H. Glenn Research Center at Lewis Field, Cleveland, Ohio 44135
and
Tina A. Karniotis Thomas**
Sherwin-Williams Company, Warrensville Heights, Ohio 44128

DOI: 10.2514/1.36549

The extended-life test of the Deep Space 1 flight spare ion thruster was voluntarily terminated on 26 June 2003. During its five-year run, the thruster operated for a total of 30,352 h, processed 235.1 kg of xenon propellant, and demonstrated extended operation at multiple throttled conditions. The objectives of the test were to characterize failure modes and quantify thruster performance as a function of engine wear and throttle level. Degradation processes included erosion of the discharge cathode keeper, accelerator-grid sputter erosion, and deposition of material in the neutralizer cathode at low power. Performance degradation was limited to a reduction in measured thrust at the full-power point for the final 1000 h of operation. Posttest inspection of the engine was initiated following the test termination to ascertain causes of the wear and to look for any previously unknown wear processes. Significant findings included facility-induced flakes in the discharge chamber, the presence of through-pits in the accelerator-grid webbing, significant erosion of the discharge cathode orifice plate, and healthy cathode inserts. A summary of the beginning-of-test and end-of-test performances and results of the posttest destructive evaluation are presented.

I. Introduction

THE Deep Space 1 (DS1) mission was launched in October 1998, on a mission to the asteroid Braille and comet Borelly. DS1 was a technology-validation mission, flying a 30-cm-diam xenon ion engine as its primary propulsion system. The ion thruster successfully completed the mission in December 2001, processing over 73.4 kg of propellant and accumulating 16,265 h of operation in space. Details on the DS1 mission performance can be found in [1,2]. The mission was a success, stimulating future NASA science missions using solar electric propulsion to demand lifetimes and propellant throughput in excess of 20,000 h and 200 kg. As a result, assessing the ultimate service-life capability of the technology is vital, requiring extensive ground testing and analysis.

An extensive ground-test program was initiated before the fabrication and testing of the flight engines. It included several endurance tests of differing durations performed on engineering model thrusters. The goals of the ground-test program were to flight-qualify the ion-thruster technology and characterize the parameters that drive potential failure and engine performance degradation. The program included 2000, 1000, and 8000 h life-demonstration tests (LDTs), all with engine operation at the 2.3-kW-power point. Several potential wear-out failure mechanisms were identified as a result of these tests and modifications were made to the flight-engine design. Details on these previous endurance tests can be found in [3–5].

Two flight thrusters were fabricated for the DS1 mission: flight thruster 1 (FT1) was mounted on the spacecraft, and the flight spare was designated as FT2. The flight spare ion thruster was the subject of an extended-life test (ELT) at the Jet Propulsion Laboratory. The ELT began in fall 1998 and was concluded in June 2003, after operating for 30,352 h, demonstrating a total impulse of 6.64×10^6 N · s and processing 235.1 kg of propellant. The objectives of the ELT were to identify previously unknown failure modes, characterize all failure modes, determine how engine performance changes with operating time, and determine the ultimate service-life capability of the NASA 30-cm-diam-ion-thruster technology.

II. Thruster Design and Operation

Details on the 30-cm-thruster design and assembly can be found in [6]. Figure 1 is a schematic of the NSTAR thruster indicating its functional components, magnetic cusps, electrical connections, and propellant inputs. Photographs of the posttest inspection throughout this paper provide views of the various subassemblies. The primary components of the NSTAR thruster are the discharge chamber, ion-optics assembly, discharge cathode assembly, and neutralizer cathode assembly.

The spun-titanium discharge chamber employs a three-ring-cusp magnetic field design. A ring of permanent magnets is located at the base of cathode assembly in the conical segment, and two rings are located, respectively, at the upstream and downstream ends of the cylindrical segment. A grit-blasted stainless-steel wire mesh is spot-welded to all surfaces in the interior of the discharge chamber (excluding the cathode assembly). This "sputter-containment" mesh was employed to prevent the formation of large flakes in the discharge chamber that could cause a grid short in the zero-gravity environment of space. Propellant is input to the thruster through

Presented as Paper 3608 at the 40th AIAA/ASME/SAE/ASEE Joint Propulsion Conference and Exhibit, Fort Lauderdale FL, 11–14 July 2004; received 10 January 2008; accepted for publication 24 August 2008.

*Senior Engineer, Systems Engineering, 4800 Oak Grove Drive, Mail Stop 301-490. Senior Member AIAA.
†Senior Engineer, Propulsion Engineering, 4800 Oak Grove Drive. Member AIAA.
‡Principal Engineer, Propulsion Engineering, 4800 Oak Grove Drive. Senior Member AIAA.
§Senior Materials Engineer, Space Environmental Durability Branch, 21000 Brook Park Road.
¶Senior Physicist Consultant, 21000 Brook Park Road.
**Research Chemist, Chemicals Group, 4440 Warrensville Center Road.

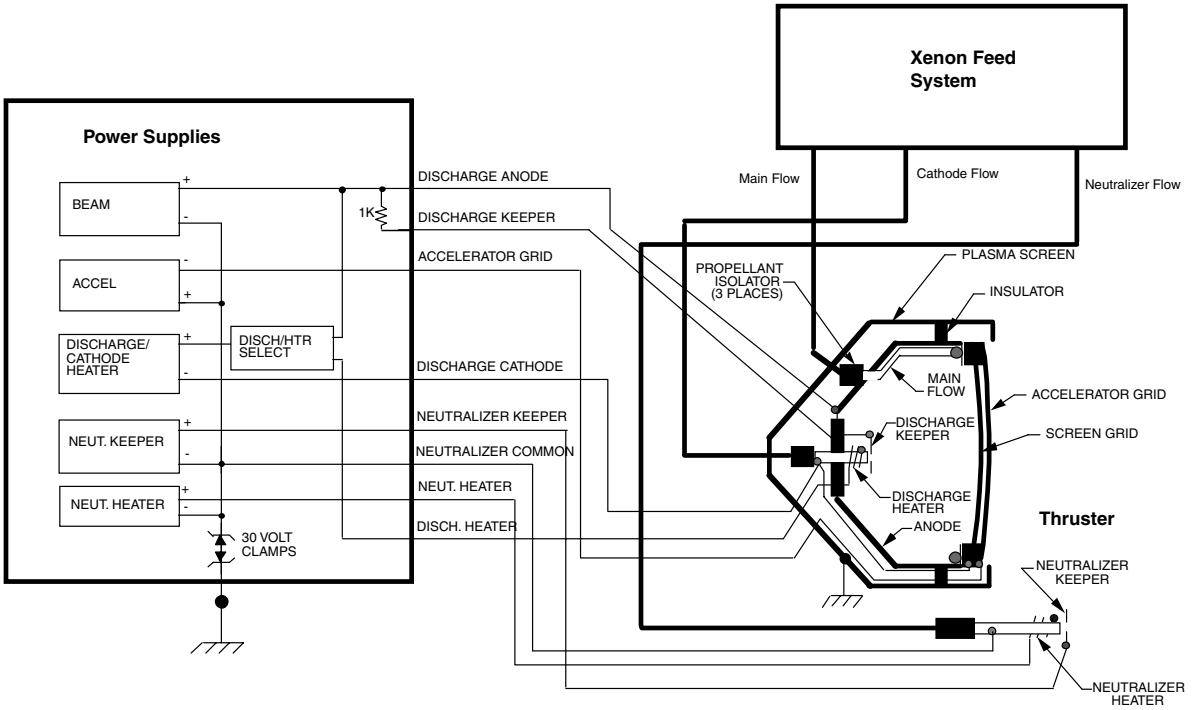

Fig. 1 Functional and electrical schematic of the NSTAR engine [8].

three locations. A propellant plenum, a perforated ring in the cylindrical segment of the discharge chamber, provides the main flow rate to the chamber. The cathode flow is fed into the discharge cathode and neutralizer flow through the neutralizer cathode. The discharge chamber is enclosed in a perforated plasma screen to prevent beam-neutralizing electrons from reaching high-voltage surfaces.

A two-grid molybdenum-optics system focuses and electrostatically accelerates the ionized xenon propellant to produce thrust. The outer accelerator grid is held at 150 to 250 V below ground potential (accelerator voltage). The accelerator-grid current refers to the current of ions that strike the accelerator grid. The inner screen grid is held at 650 to 1100 V above ground potential (beam or screen voltage). The screen-grid current refers to the current of discharge chamber ions that strike the grid.

An impregnated-tungsten hollow cathode in the discharge chamber serves as the electron source for xenon ionization. The discharge cathode range of operation is 5 to 15 A and 2.5 to 3.7 sccm of xenon for nominal NSTAR operation. A coiled-tantalum sheath heater and keeper electrode are used to ignite the cathode. A second impregnated hollow cathode, located on the exterior of the discharge chamber is used to charge-neutralize the ion beam. As with the discharge cathode, a sheath heater and keeper electrode are used for ignition. The neutralizer cathode range of operation is from 1.5 to 2.4 A and 2.4 to 3.6 sccm of xenon.

III. Test Facility and Plan

The test was conducted in a 3-m-diam by 10-m-long vacuum chamber with a total xenon-system pumping speed of 100 kl/s. The vacuum system provided a base pressure of less than 5.3×10^{-4} Pa at the full-power flow rates. The pumping surfaces were regenerated after accumulation of 10 kg xenon, during which time the engine was exposed to a mostly xenon background pressure of 133.3 Pa. The vacuum chamber was lined with graphite panels to reduce the amount of material backsputtered onto the engine and test diagnostics. The propellant-feed system consisted of two mass-flow meters in series for each of the cathode, neutralizer, and main lines. Laboratory power supplies, with similar capabilities to the DS1 flight power processing unit, were used to run the thruster. A computer data-acquisition system was used to monitor the engine and test facility. Details on the test facility and electrical system can be found in [7–9]. Several diagnostics were used to measure the ion-beam characteristics as well as general engine performance parameters. The diagnostics included a thrust stand, $E \times B$ probe, thrust-vector probe, Faraday probe, video-camera system, laser profilometer, and retarding potential analyzer. Specific details on the operation and design of the diagnostics can be found in [7–9].

The thruster was designed to be throttleable to maximize use of available solar array power in space. The DS1 thruster used a total of 50 throttle levels out of the 112 levels available; however, for the ELT, 16 throttle points were chosen to facilitate testing. The throttle table used a TH designation for each operating point, with a power range of 0.5 kW (TH0) to 2.3 kW (TH15), the minimum- and full-power points, respectively. The throttle table can be found in [7]. The beam current and voltage were actively controlled to provide different fixed levels of thrust and specific impulse. A current-regulated discharge cathode power supply was controlled to produce the ions required to provide the desired beam current. A voltage-regulated power supply was used to control the beam (screen-grid) voltage. For each throttle point, flow rates were set to account for the higher neutral density in the vacuum chamber (relative to space) and to maintain a propellant-use efficiency of approximately 90%. Propellant-use efficiency is the ratio of beam current produced to the total mass-flow rate into the engine and cathodes. The neutralizer flow rate was set to minimize cold-flow losses while providing a sufficient margin from plume-mode operation.

FT2 was operated primarily at only 5 of the 16 throttle points (TH0, 5, 8, 12, and 15) for approximately 5000 to 6000 h intervals to investigate wear and failure as a function of power level. Table 1 indicates the power level, propellant processed, duration for each test segment, and cumulative operating time. There was an emphasis on full-power operation to maximize propellant throughput, because accelerator-grid wear is most significant at this level, as will be shown in Sec. IV.E. Operations at 0.5 kW (TH0) and 1.46 kW (TH8) were chosen to investigate potential wear and failure mechanisms at the throttled conditions. Operation at TH5 was specifically chosen to support the Dawn mission, to understand neutralizer performance degradation at the power level planned for the transfer from Vesta to Ceres [10]. During each test segment, thruster electrical parameters were monitored and recorded every 5 s by a computer-based data-acquisition system. The location of the thrust vector was recorded every 5 min, and performance data were obtained every 100 to 200 h.

Table 1 Test-segment summary

Parameter	Test segments						
Throttle level	TH12	TH15	TH8	TH15	TH0	TH15	TH5
Power, kW	2.0	2.3	1.5	2.3	0.5	2.3	1.1
Throughput, kg	3.9	44	39.7	54.3	22.4	46.5	24.3
Segment duration, h	447	4246	5758	5166	5689	4400	4646
Cumulative duration, h	447	4693	10,451	15,617	21,306	25,706	30,352

The remaining throttle points were only investigated during short-duration performance testing. The performance tests, in conjunction with neutralizer characterizations and sensitivity tests, were performed every 2000 to 3000 h to investigate engine performance and wear over the full throttle range. Video and photographic data of the neutralizer and discharge cathode assemblies and downstream face of the accelerator grid were taken with a video-camera system inside the vacuum chamber to monitor and quantify erosion processes. These video analyses were made every 1000 to 2000 h.

The posttest analyses were initiated immediately following final engine shutdown. The destructive analyses were performed at the component level, documenting wear and deposition sites for the discharge chamber, discharge cathode assembly, neutralizer cathode assembly, and ion-optics assembly. Wear was quantified by a combination of optical inspection, scanning electron microscope (SEM) inspection, energy dispersive x-ray analysis (EDX), and both noncontact and contact physical measurements. The posttest analyses also included a determination of facility-induced effects on wear and engine performance.

IV. Results and Discussion

A. Overall Engine Performance

The thrust F_{th} and total engine efficiency η_T were measured continuously over the engine's five years of operation. Thrust is proportional to the product of the beam current and square root of the beam voltage. Beam voltage V_B and current J_B were actively controlled during the test; therefore, variations in thrust under normal operating conditions can only be due to variations in double-ion content of the beam and variations in beam divergence:

$$F_{\text{th}} = \alpha F_T J_B \sqrt{(V_B - V_G)} \sqrt{\frac{2M_i}{e}} \tag{1}$$

$$\eta_T = \frac{F_{\text{th}}^2}{2\dot{m}P_{\text{in}}} \tag{2}$$

where coefficients α and F_T correct for the double content and nonaxial ion velocity loss, respectively, and coupling voltage V_G, xenon ion mass M_i, electron charge e, and engine input power P_{in} are all known or measured quantities [11].

Figures 2 and 3 compare the measured thrust and efficiency versus engine power level at the beginning of life (BOL) and after 30,352 h of operation. The engine thrust and efficiency degraded by less than 4 and 9%, respectively, from the BOL values for the entire throttle range. Thrust degradation at 2.3 kW (TH15) was primarily due to unpreventable electron backstreaming, which occurred during the last 1000 h of operation, only at the full-power point. Electron backstreaming resulted in a reduction in beam current, thereby reducing thrust. Before the onset of unpreventable electron backstreaming, TH15 had only degraded by 3%, which is within the uncertainty of the thrust-stand measurement. Temporal variations in thrust at power levels between 0.5 and 2 kW are not fully understood, though they may be due to slight increases in double-ion content or beam divergence. Total efficiency degraded primarily due to increased discharge power requirements, likely due to cathode insert depletion and increased neutral loss via grid aperture enlargement. The specific impulse of the thruster was calculated as a function of run time and power level and degraded by less than 9% by the conclusion of the test. A complete review of the in-test engine performance at all of the power levels investigated can be found in [7].

B. Discharge Chamber Performance

1. In-Test Performance

Discharge voltage, discharge current, and flow rates were monitored to track discharge chamber performance as a function of time. During the first 15,000 h of the test, there was a trend to increasing discharge current over the entire throttle range, with the rate being highest when the thruster was operating at 2.3 kW. Increased neutral loss due to accelerator-grid aperture enlargement is believed to be responsible for this trend. From 15,000 h through the conclusion of the test, discharge current was stable and relatively constant over the full throttle range. Discharge current variations were negligible during the TH0 and TH5 test segments and actually decreased slightly during the TH8 test segment.

FT2 operated with a discharge voltage range of 23.1 to 26.4 V. This range of operation limited double-ion production while maintaining a discharge chamber propellant-use efficiency of greater

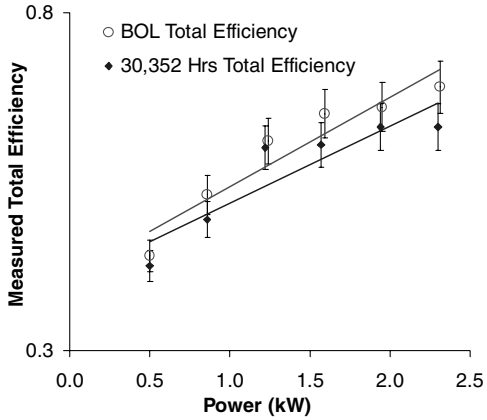

Fig. 2 Comparison of measured total efficiency versus power level at the beginning and end of the test. The experimental data are indicated by markers. A linear curve fit is overlaid for each data set.

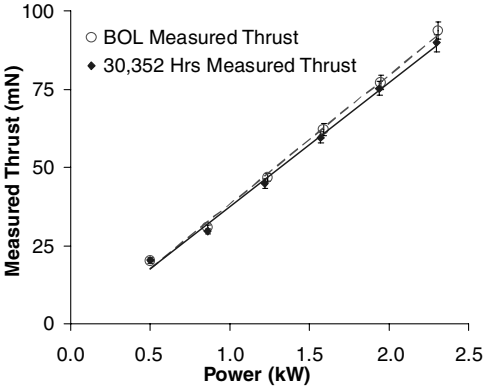

Fig. 3 Comparison of measured thrust versus power level at the beginning and end of the test. The experimental data is indicated by markers. A linear curve fit is overlaid for each data set.

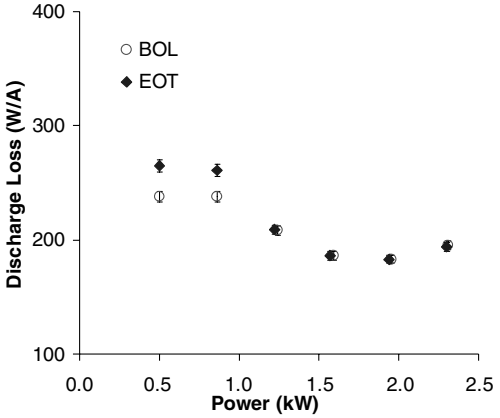

Fig. 4 Comparison of measured discharge loss versus power level at the beginning and end of the test. The experimental data are indicated by markers. A linear curve fit is overlaid for each data set.

than 90%. The TH8 and TH5 segments exhibited the highest discharge voltages of 25 to 26.4 V, as compared with TH15, which operated on average below 24 V. The variation with power level was due in large part to the high sensitivity of the discharge voltage to the main and cathode flow rates. Sensitivity data at the TH15 throttle point indicate that discharge voltage dependence on main and cathode flow rates outweighed the dependence on beam current, leading to a lower discharge voltage at TH15.

Discharge loss was also monitored to track discharge chamber performance over time. Discharge loss ε_b is the product of the discharge current J_D and voltage V_D divided by the beam current:

$$\varepsilon_b = \frac{J_D V_D}{J_B} \tag{3}$$

The discharge loss is a measure of the amount of energy expended in producing and extracting a single beam ion. Figure 4 is a comparison of discharge loss versus power level at BOL and after 30,352 h of operation. The beam-ion energy cost varied by less than 1% from BOL through the conclusion of the test, further demonstrating the excellent condition of the discharge chamber and discharge cathode after 5 years of operation. More details on the in-test engine performance can be found in [7–9].

2. *Posttest Inspection*

Posttest inspection of the engine discharge chamber immediately following removal from the vacuum chamber revealed the presence of numerous flakes on the surface of the sputter-containment mesh (Fig. 5). The majority of the flakes were less than 0.1 mm in length, although a few large flakes were on the order of 1 mm in length. SEM analysis of the less than 0.1-mm-long cross-sectioned flakes revealed a three-layer structure of molybdenum–carbon–molybdenum. The atomic composition of the flakes ranged from 40 to 70% carbon and 30 to 1% molybdenum, with trace amounts of tantalum and stainless steel. The sources of molybdenum are the screen grid and discharge keeper electrode plate, the tantalum is from the keeper tube and discharge cathode heater, and stainless steel is from any exposed bolt heads. Although the flakes varied in composition, they were largely of carbon composition, suggesting that the flakes are a facility-induced effect and would not have formed if the engine were operated in space. The extensive carbon deposition found to be on many of the thruster's interior and exterior surfaces is a direct result of the redeposition of sputter-eroded carbon atoms from the graphite panels that line the vacuum chamber. A crude total-mass estimate of the flakes found on the bottom of the discharge chamber is 21 mg $\pm$ 5 mg. An extensive statistical and chemical analysis of the discharge chamber flakes can be found in [12].

SEM analysis of the sputter-containment mesh also indicates the presence of deposits with varying thicknesses and compositions as a function of distance from the screen-grid electrode (Fig. 5 bottom). The sputter-containment mesh is a stainless-steel weave designed to collect sputter-deposited material and make it adhere to itself; the deposits are 5 to 15 μm thick and exhibit a layered structure corresponding to variations in molybdenum (Mo) versus tantalum (Ta) and stainless content. Representative elemental compositions of the mesh deposits are plotted in Fig. 6 for six different axial locations extending from the rear of the chamber near the cathode plate to the near-screen-grid region. The containment-mesh film thickness is 10 to 15 μm near the screen grid with a composition of 80% molybdenum, 8% carbon, and 10% tantalum. The thickness near the cathode is less than 5 μm on average, with a composition of

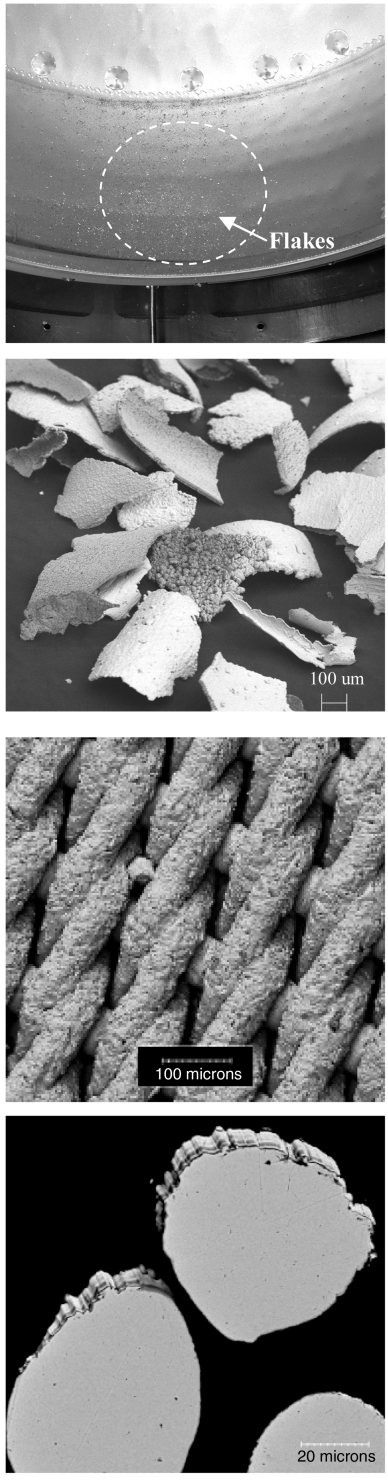

Fig. 5 Discharge chamber sputter-containment mesh with flakes (top), discharge chamber flakes (upper middle), top surface view of near-cathode sputter-containment-mesh sample (lower middle), and cross-sectional view of mesh sample wires with film adhered to it (bottom) .

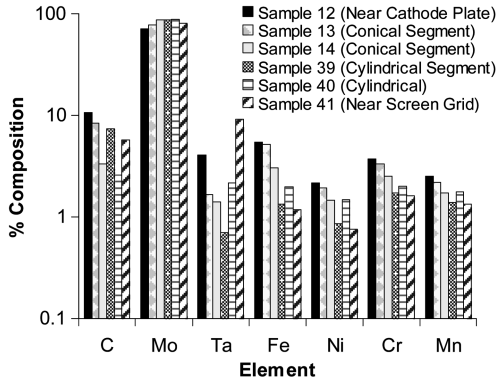

Fig. 6 Sputter-containment-mesh thin-film elemental atomic percent composition for different axial locations plotted on logarithmic scale.

70% molybdenum, 11% carbon, and 5% tantalum, with the remainder being stainless steel and trace elements. There was no apparent azimuthal variation in thickness or composition for a given axial location, suggesting that gravity did not influence the extent of deposition or adherence to the mesh. Inspection of the deposited films indicate that they had not yet bridged the gaps between the weave, a criterion used for the adequate retention of sputter-deposited films.

A gauss meter was used to measure the internal magnetic field of the engine after the grids were removed. Figure 7 is a plot of the centerline magnetic field strength at BOL and after 30,352 h of operation. There was no measurable degradation in the internal discharge chamber magnetic circuit throughout the interior of the discharge chamber, which corresponds to the absence of change in the discharge performance from BOL. The external magnetic field was also mapped, using a Helmholtz coil and magnetometer boom. Comparison of this data with pretest data indicated no change in the external field strength.

Posttest inspection of the high-voltage propellant isolators was also performed to determine any possible degradation in isolation performance from BOL. High-voltage vacuum testing of both the main and discharge cathode high-voltage propellant isolators was performed to measure breakdown voltage as a function of upstream internal pressure. Upstream pressures representative of the full-power flow rate throttle range were investigated. Comparison of the 30,000 h isolators and an unused control isolator of the same design indicated virtually identical breakdown performance over the full range of pressures. Reference [13] contains a detailed overview of the posttest analysis of the discharge chamber.

C. Discharge Cathode Performance and Wear

1. *In-Test Performance*

The ELT discharge cathode operated for a total of 30,472 h and was ignited (cycled) 277 times, establishing the ELT as the longest endurance test of a hollow cathode to date. The most significant wear mechanism experienced by the cathode assembly during operation was sputter erosion of the keeper electrode plate (Fig. 8). Discharge cathode keeper erosion is a wear mechanism for ion thrusters, as demonstrated by the previous 8200 h test (LDT) of an engineering model thruster (EMT2) and the extended-life test of FT2 [3,7]. After 15,000 h of operation, the keeper on FT2 eroded sufficiently to fully expose the cathode heater and cathode orifice plate to the discharge plasma for the remaining 15,000 h of the test. Keeper erosion was first observed during the TH8 test segment, following a short between cathode keeper to cathode common at 5850 h. At that point, the keeper began to erode at an observable rate. The intermittent short cleared when the cathode keeper orifice plate eroded sufficiently to remove it. Cathode keeper erosion continued, however, at the subsequent full-power segments, and at a lower rate during TH5 operation.

It is important to note that keeper erosion of this severity was not observed during the first full-power test segment, from 500 to 4500 h, or during the previous 8000 h endurance test of the engineering model thruster [5], which was operated exclusively at TH15. This suggests that the TH8 operating conditions, the shorted condition, or both, initiated the severe cathode keeper erosion observed during FT2 testing. In spite of the keeper erosion and subsequent exposure to the discharge plasma for 15,000 h, the cathode did not experience any measurable change in its ignition voltage over time for the duration of the test. Therefore, as will be discussed in the subsequent section, the performance of the cathode heater, orifice, and insert was not compromised.

2. *Posttest Examination*

Posttest inspection of the discharge cathode assembly has been subdivided into detailed analysis at the subcomponent level. Detailed materials analysis and optical inspection of the cathode orifice plate, insert fracture surface and inner diameter, cathode tube, cathode

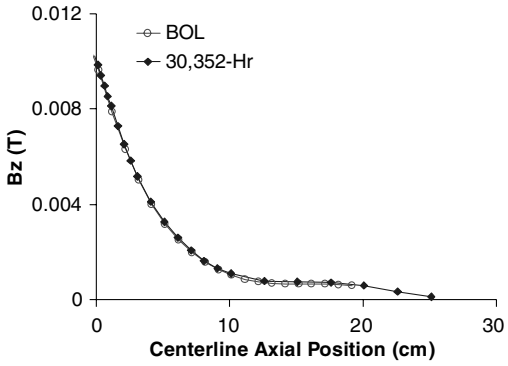

Fig. 7 Comparison of BOL and 30,352 h centerline magnetic field strength.

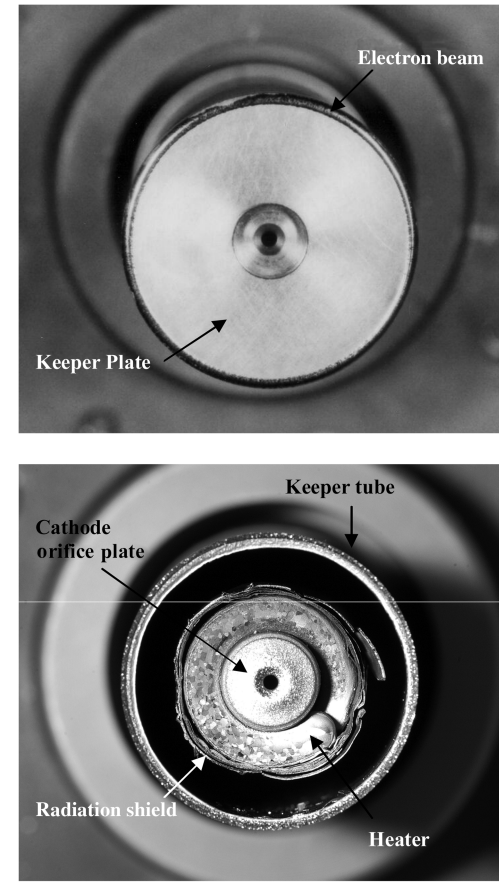

Fig. 8 Discharge cathode assembly at the beginning of the test (top) and at the conclusion of the test after 30,352 h (bottom). The cathode keeper plate was completely removed at the EOT.

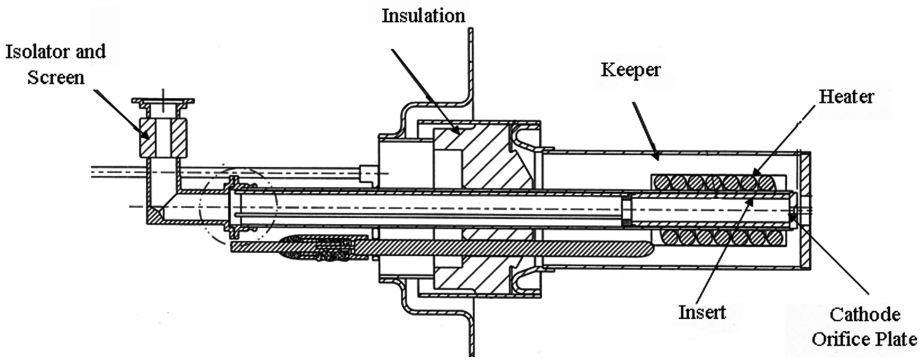

Fig. 9 Schematic of the discharge cathode assembly [14].

heater, cathode keeper, and low-voltage propellant isolator were performed (Fig. 9). EDX and SEM analysis are used to determine the extent of regions of net deposition and erosion, and their composition. Laser-profilometer scans of the cathode orifice plate surface have also been obtained to quantify mass loss and eroded depth. The critical findings to date will be discussed in the subsequent sections.

Posttest examination of the cathode assembly confirmed that the keeper plate had been fully removed by ion bombardment from the discharge plasma. Figure 8 shows the BOL and EOT (end-of-test) condition of the assembly. In addition to removal of the keeper plate, the cathode orifice plate, cathode heater, and radiation shield, and cathode keeper tube all experienced measurable sputter erosion due to exposure to the discharge plasma.

Posttest examination of the cathode indicated surface erosion of the orifice plate was more severe than previously surmised from the in situ video-camera photography during the course of the test. The connection of the cathode orifice plate to the cathode tube is a circumferential electron-beam weld joint. The weld was completely removed by ion bombardment sputter erosion of the plate surface by the conclusion of the test (Fig. 10). By the conclusion of the test, the periphery of the plate was only 28% of the pretest plate thickness. Although the weld joint was fully removed by sputter erosion, the orifice plate was still adhered to the cathode tube wall and ledge at the conclusion of the test. SEM analysis indicated this adherence was due to a 20- to 50-μm-wide area of fusion between the moly-rhenium (MoRe) cathode tube and tungsten (W) orifice plate. If not for this small area of thermally induced fusion, the plate may have fallen off, resulting in cathode failure. This is a key finding of the ELT, showing that minimizing cathode keeper erosion to prevent ion bombardment of the orifice plate is essential to prevent premature cathode failure. A three-dimensional contour plot of the orifice plate surface was obtained by laser-profilometer scans across the surface. Depth data obtained from the profiles scans indicated that approximately 50% of the tungsten plate had eroded after 30,000 h of operation. In contrast to the surface erosion, the plate's orifice channel and chamfer did not experience any net erosion.

Examination of the upstream side of the cathode orifice plate revealed heavy deposition of tungsten on the plate surface and inside the orifice channel (Fig. 11). The deposits reached a maximum thickness of 50 μm on the channel wall and decreased in density and thickness with radial distance from the orifice.

Examination of the discharge cathode tube revealed a significant quantity of barium oxide (BaO) on the inner diameter surface. The source of the BaO is the insert impregnate material, which had fused to the interior surface of the cathode tube. The trend noted was increasing BaO deposition in the downstream direction, which corresponds to the higher temperature.

Posttest examination of the discharge cathode keeper tube revealed the presence of large tantalum deposits fused to the interior of the downstream tube wall as shown in Fig. 12. The source of the tantalum deposits is believed to be flaking of the discharge cathode heater radiation shield, as shown in Fig. 13. Flaking likely began after erosion of the cathode keeper plate exposed the radiation shield to the main discharge plasma. These flakes are up to 2 mm in length, and of sufficient size to cause a grid-to-grid short and/or severe ion impingement of the accelerator grid if deposited on the upstream screen-grid surface. The flaking of the radiation shield, a direct result of keeper erosion, represents a previously under appreciated failure mechanism, which could potentially lead to an unclearable grid-to-grid short or rogue hole formation on the accelerator grid.

Posttest examination of the cathode heater revealed significant sputter erosion and Ta crystallite growth on the surface of the downstream coil. The source of the crystallites is redeposited heater-sheath material. The last heater coil exhibited surface cracking in several locations, but no exposure of the MgO insulator was detected anywhere in the eroded region. The heater was energized under vacuum, its thermal response monitored with an infrared camera. Comparison of the infrared mapping data of the 30,000 h discharge heater and a control heater, showed very little difference in both transient and steady-state performance at 3 A. In addition, temperature variations along the heater were less than 50°C,

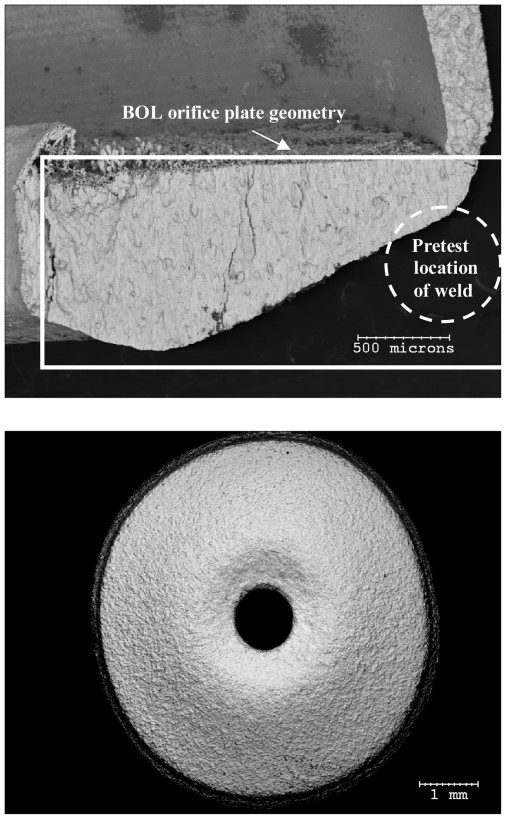

Fig. 10 Cathode orifice plate after 30,352 h of operation: cross-sectional view (white box indicates the BOL condition and location of the cathode plate-to-tube weld) and downstream surface of the cathode orifice plate at the end of the test (bottom).

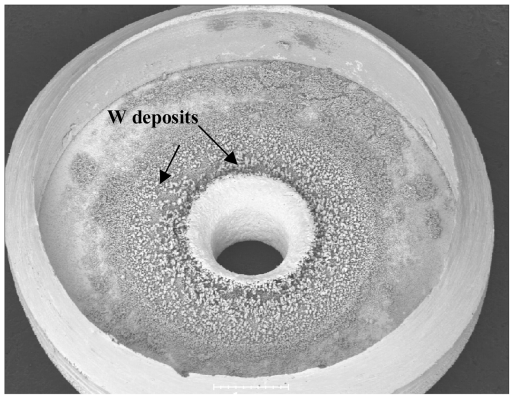

Fig. 11 Posttest condition of the upstream side of the cathode orifice plate. Radial variation in tungsten deposits around the orifice is apparent.

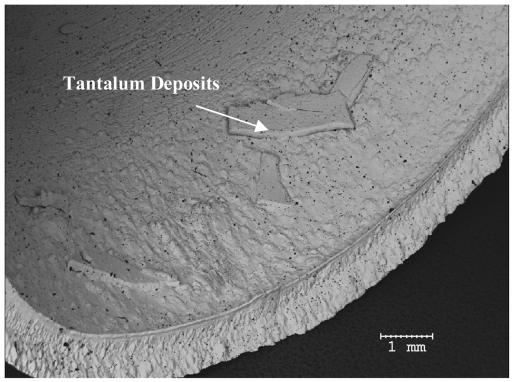

Fig. 12 Discharge cathode keeper tube interior showing millimeter-sized tantalum deposits adhered to the surface.

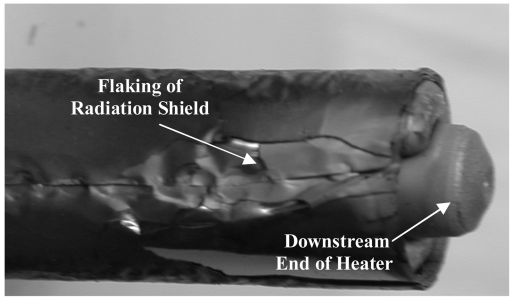

Fig. 13 Posttest condition of the cathode heater radiation shield indicating flaking of the foil material. Erosion of the downstream end of the cathode heater is also apparent.

confirming the heater operation and internal structure had not been compromised.

Posttest examination of the low-voltage propellant isolator assembly revealed evidence of arcing and high-temperature operation in the feed-line connections and ceramic as shown in Fig. 14. Arc tracks and melting were also evident on the discharge propellant line screen, located just upstream of the isolator (Fig. 14). It is believed an electrical discharge through the isolator was responsible for this arc damage. The low-voltage isolator is designed to reliably stand off ~100 V, and in normal operation it must stand off the cathode-to-anode potential of approximately 25 V, which is well within its capability. During the ELT, the voltage used to start the cathode was nominally 250 V, although a flightlike start circuit that produced 650 V pulses was used at the beginning of the test. Therefore the nominal start voltage was in excess of the design limit of the isolator. It is likely that arcing occurred at these voltages, hence

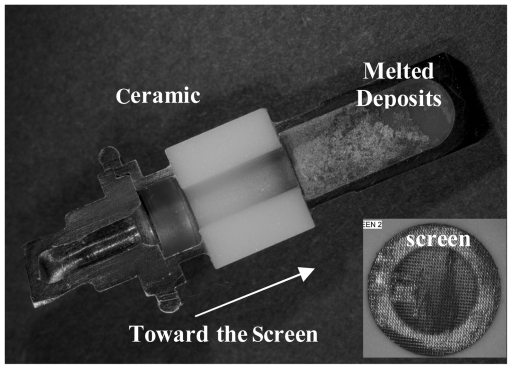

Fig. 14 Cross section of the discharge cathode low-voltage propellant isolator showing arcing and deposition in the feed-line connection and ceramic. The lower right insert shows the propellant line screen with arc tracks.

that observed in the posttest examination. SEM examination of the ceramic to propellant line braze indicates that braze material did flow due to arc induced heating, but it was not sufficient to result in failure of the braze joint. Posttest inspections of the ceramic revealed a submicron-thick coating of nickel and braze material along the entire length of the ceramic. This is critical, because during the five years of operation, the impedance between cathode and anode varied dramatically from 2 GΩ at the beginning of the test to 1 MΩ at the end. It is likely that this layer of redeposited nickel and copper provided a conductive path from cathode common to anode, which manifested itself during the test as a variable impedance between these two electrical connections.

3. *Insert Analysis*

A detailed analysis of the fracture surface of the discharge cathode insert was performed. The insert is a thermionic emitter consisting of a porous tungsten-matrix impregnated with a compound mixture of barium oxide, calcium oxide, and alumina (BaO-CaO-Al2O3) with a stoichiometric coefficient ratio of 4:1:1. SEM and EDX analysis of the fracture surface of the 30,000 h insert and an unused 4:1:1 insert, were used to characterize the condition of the surface, and provide a comparative estimate of the amount of impregnate material present as a function of depth from the surface and in the axial direction (upstream/downstream) [14]. SEM inspection of the insert revealed heavy tungsten deposition at the extreme downstream end nearest the orifice plate, but the absence of any tungsten oxide or barium oxide layers on the entirety of the surface (Figs. 15 and 16). This is a critical finding, as oxide layers are typically responsible for limiting cathode life by preventing BaO migration to the surface [15]. Impregnate depletion was maximum at the surface and most apparent at the downstream end of the insert. The relative EDX signal strengths for barium (Ba) and tungsten (W) were obtained for both the unoperated insert and the 30,000 h insert as a function of depth from the inner diameter (ID) surface. This comparative approach provides a semiquantitative measure of relative impregnate depletion, which can be used to ascertain the operable condition of the emitter surface and may be used to extrapolate life. Figure 17 is a plot of the Ba/W ratio for the unoperated sample insert and the downstream end of 30,000 h insert, from 100 to 500 μm from the ID surface. The ID surface of the 30,000 h insert exhibited approximately 50% of the signal strength for impregnate material relative to the unoperated insert. The nonlinear profile of barium concentration with depth from the ID surface of the unoperated insert is likely related to its initial processing. This is consistent with the neutralizer insert barium profile, to be shown in a subsequent section. The barium profile for the discharge insert showed degradation at the ID surface and subsurface. At 500 μm from the ID surface, the impregnate material signal strength was roughly equivalent to the unoperated insert. This suggests that after 30,000 h of operation, the quantity of impregnate material at the surface was reduced, but still available for diffusion from the subsurface. This allowed the cathode to operate as an

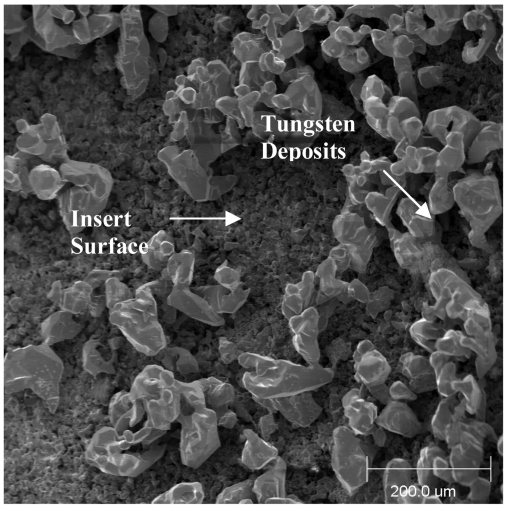

Fig. 15 Downstream end (closest to the keeper) of the discharge cathode insert surface showing tungsten deposits on the tungsten matrix substrate.

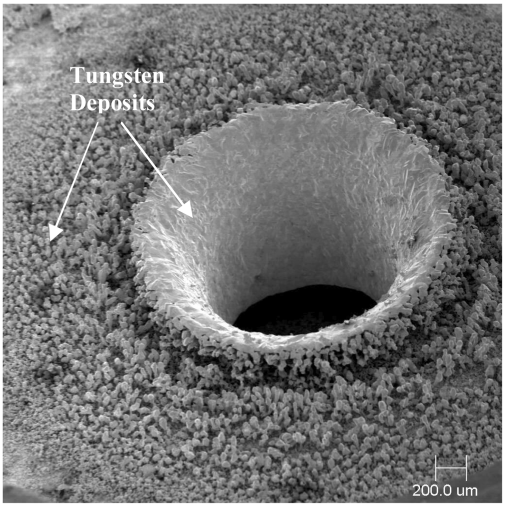

Fig. 16 Discharge cathode orifice plate upstream surface showing tungsten deposits and their radial variation.

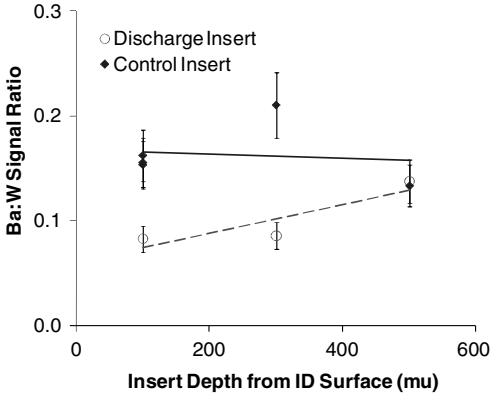

Fig. 17 Discharge cathode insert Ba/W ratio measurement comparison for an unused 4:1:1 insert and the ELT insert after 30,352 h of operation.

electron emitter through to the end of the test. In addition, the Ba/W ratio measurements represent a worst-case measure of remaining insert life, as impregnate depletion at the downstream end of the insert was the most severe.

The comparative analyses confirm the absence of any oxide or poisoning layers on the insert surface which is consistent with the nominal in-test performance. Therefore it is likely that the discharge insert had not yet reached the end of its useful life.

D. Neutralizer Cathode Performance and Wear

1. In-Test Performance

The neutralizer cathode is the source of beam-neutralizing electron current to prevent spacecraft charging. The neutralizer is a hollow cathode, with xenon gas as the neutral source. The cathode is housed inside a cylindrical keeper electrode assembly that serves as the anode. For FT2 testing, the keeper power supply maintained the neutralizer current at the fixed level specified in the NSTAR throttle table [8]. The neutralizer keeper voltage was dependent on the flow rate of xenon through the cathode, the condition of the orifice, and the keeper current. Nominal operation of the neutralizer is called spot mode, in which the voltage oscillations of the keeper are significantly less than 5 V peak to peak. Plume mode occurs when the cathode sheath extends to the anode, resulting in large voltage oscillations, an increase in dc voltage, and the production of energetic ions that may have sufficient energy to erode neutralizer surfaces, reducing the lifetime and performance of the neutralizer cathode. The flow rate margin from plume mode is defined as the number of sccm of xenon required to operated above plume-mode operation. Operating with sufficient flow rate margin and keeper current can prevent plume-mode operation and, as such, the performance of the neutralizer was closely monitored during the course of the test.

Neutralizer keeper performance characteristics were relatively stable during the TH15, TH8, and TH5 test segments. The neutralizer performance first began to show signs of degradation during the TH0 (0.5 kW) segment: the dc and ac characteristics began to increase 800 h into TH0 operation, and deposits began to form within the orifice. By the conclusion of the TH0 segment, which lasted for 5700 h, internal-tank video inspections revealed that the orifice was over 50% blocked, and the flow rate margin from plume mode had dropped to below acceptable levels at the nominal flow rate set point. As shown in Fig. 18, deposits began to form inside the orifice of the neutralizer during this period of operation. The thruster was returned to full-power operation following the TH0 test segment and remained at the TH15 power point for approximately 5000 h. During this test segment, the deposits within the orifice were removed, and the TH0 keeper voltage characteristics and flow rate margin from plume mode returned to nominal levels [8]. This suggests that operation at the higher power level removed the deposits and that the deposition mechanism is likely power-level-dependent, specifically manifesting itself during low-power operation.

A similar phenomenon was observed during the DS1 mission, in which the flight neutralizer exhibited signs of plume-mode operation following extended operation at 0.54 kW (∼TH0). Extensive ground and in-flight tests with the respective engines were performed at that time to characterize the flow rate and keeper current dependence on plume-mode operation. Analysis of data from the retarding potential analyzer diagnostic available both on the DS1 spacecraft and in the ELT test facility indicated that increasing keeper current and/or increasing flow rate through the neutralizer will reduce energetic ion production and increase margin from plume-mode operation. Based on these results, the neutralizer flow rate was increased for DS1 low-power operation, and neutralizer keeper current was increased for the final ELT test segment at TH5 (1.1 kW). The TH5 power level was specifically chosen to investigate the power-level dependence of neutralizer performance degradation. Details on these tests can be found in [16].

Impedance degradation between the neutralizer keeper to ground and neutralizer common to keeper was also observed over the 30,000 h of operation. The impedance for both of these paths decreased from 10 GΩ to the ∼MΩ range during the first 2000 h of operation. For the remainder of the test, impedance between these two paths continued to decrease, with the rate of decrease scaling directly with power level. By the conclusion of the test, the impedance between keeper and ground was 40 kΩ and common to

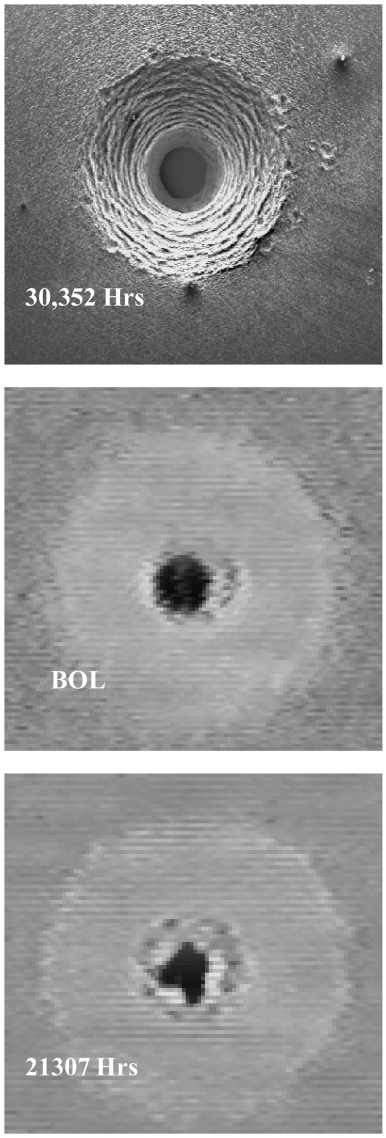

Fig. 18 Neutralizer cathode orifice images at different operating times showing the formation and subsequent removal of deposits in the orifice.

keeper was 0.6 MΩ. It is important to note, however, that the impedance reduction did not negatively affect neutralizer cathode ignition or operation during the five years of operation. The causes of these impedance degradations are discussed in the next section. Details on the impedance trends during the test can be found in [7,8].

2. Posttest Inspection

Posttest inspection of the neutralizer cathode assembly has yielded several findings with regard to net erosion and deposition on key subassemblies. The posttest inspection includes detailed materials and physical analysis of the keeper tube and plate, orifice plate and channel, insert fracture surface, ceramic insulator, and heater. Key findings will be presented in the following sections.

Posttest examination of the neutralizer keeper tube wall thickness indicates that the side with direct line of sight to the exhaust beam had eroded up to 20% from the nominal wall thickness at the downstream end (Fig. 19). This erosion is proportional to the square of the beam voltage, providing a potential failure mode for higher-specific-impulse thruster designs. The nonexposed side of the keeper tube and the downstream face of the keeper plate had a primarily carbon coating up to 20 μm thick, both the result of the redeposition of facility material in the thruster plane. The upstream side of the neutralizer keeper plate had a partially flaking submicron-thick coating of stainless, carbon, and tungsten deposited over the entire

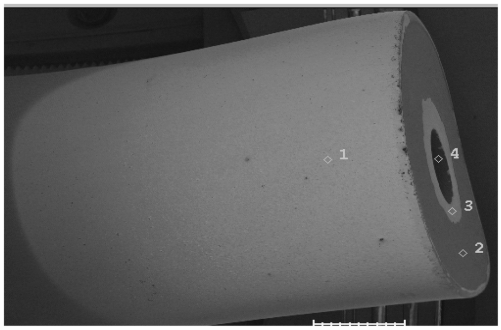

Fig. 19 Neutralizer keeper tube erosion of the beam-exposed side with a graph of wall thickness versus axial position overlaid.

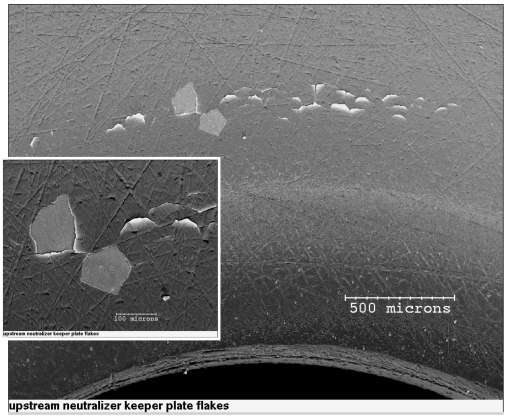

Fig. 20 Neutralizer keeper plate upstream deposits and flaking.

surface (Fig. 20). Semiquantitative analysis of the coating indicated that it is 80% carbon and therefore primarily a facility-induced effect.

SEM inspection of the aperture in the neutralizer keeper plate also revealed the presence of net deposition (Fig. 21). The two-layer deposit was composed of a dense tungsten layer, followed by a much thicker but less dense tungsten-follicle layer. Comparison of the posttest condition of the ELT keeper aperture to the LDT aperture indicates a similar dense tungsten layer, but an absence of the tungsten follicles found in the ELT keeper plate orifice. These follicles may be related to or similar in composition to the deposits observed in the neutralizer cathode orifice during the TH0 test segment.

SEM inspection of the neutralizer orifice plate and channel revealed the absence of erosion in the thickness dimension and no evidence of the deposits that clogged the orifice previously photographed during the TH0 test segment (Fig. 22). The orifice exhibited net erosion of the orifice channel, as seen in Fig. 22 (top). Comparison of the net erosion of the 30,352 h ELT to 8000 h LDT neutralizer orifice indicates that the profile and magnitude are remarkably similar [3]. This suggests that neutralizer orifice erosion essentially stops after achieving this eroded geometry. Although deposits formed within the orifice during the TH0 segment, these were removed by subsequent TH15 operation and the erosion profile returned to the posttest condition shown in Fig. 22.

The upstream surface of the cathode orifice plate exhibited a ring of BaO particles, consistent with where the insert cylinder contacted the plate. A few tungsten particles were also found on the surface, but, in general, the plate was clean, in stark contrast to the discharge cathode orifice plate.

Posttest inspection of the neutralizer cathode heater and radiation shield indicated no sputter erosion of either part. Infrared vacuum testing was performed, and the energized neutralizer heater performed similarly to a control heater with regard to transient and steady-state performance at 3 A of current. Temperature variations on the heater and over the individual coils were less than 50°C.

Posttest inspection of the neutralizer insulator is focused on understanding the cause of the impedance degradations experienced

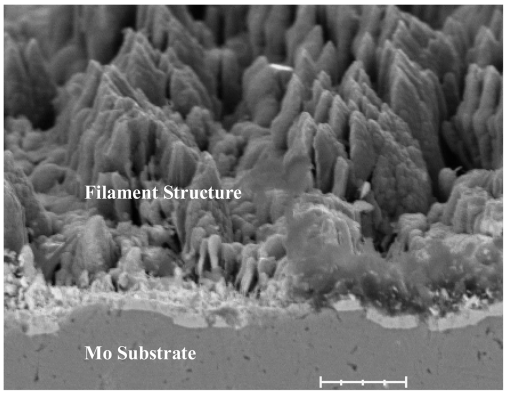

Fig. 21 Neutralizer keeper aperture deposit structure.

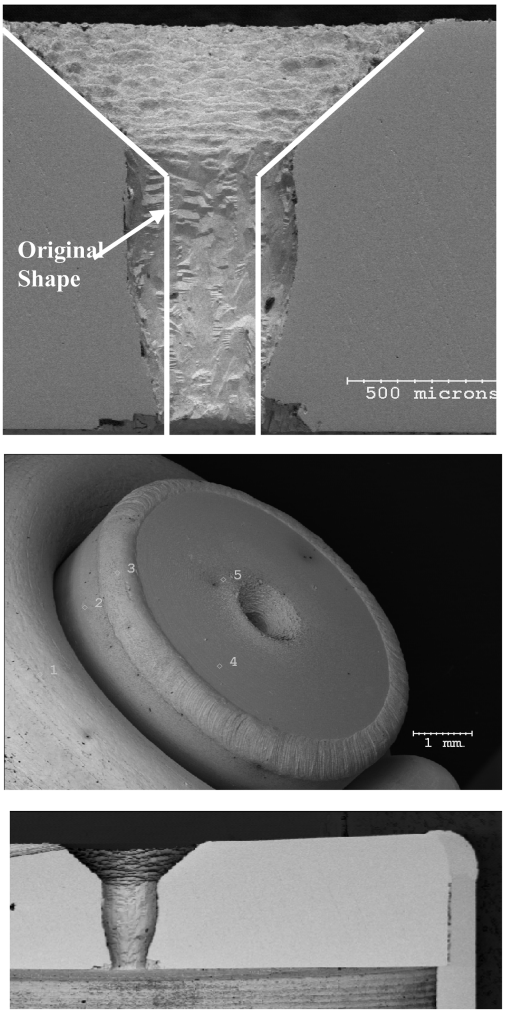

Fig. 22 Neutralizer cathode orifice posttest images: cross section of orifice and chamfer indicating erosion (top), downstream surface of the orifice plate and last coil of the heater (middle), and cross section of the orifice plate also showing the cathode tube interior (bottom) .

during the test. Minimal but measurable sputter deposition of tantalum and MoRe from the cathode and keeper tubes was found on the downstream surface of the ceramic in the vicinity of the cathode tube. These deposits did not extend to the surrounding keeper tube and therefore did not provide a conductive path to the keeper electrode. A submicron layer of carbon, however, was found on the downstream surface of the ceramic, and a conductive path from the central cathode tube to the surrounding keeper tube is visible in Fig. 23. Although the coating was too thin to quantitatively measure its thickness with EDX analysis, a resistivity calculation made along

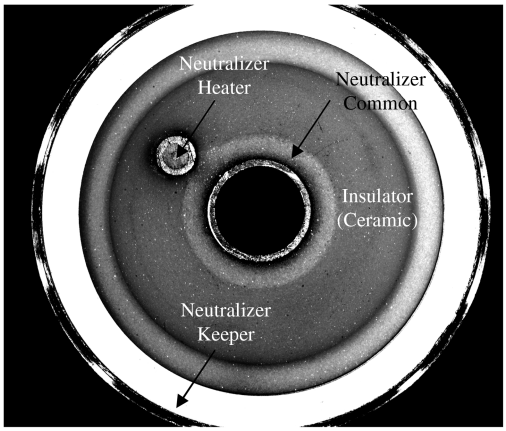

Fig. 23 High-contrast image of neutralizer insulator ceramic highlighting carbon deposition on the surface.

the conductive path indicates that a carbon coating on the order of 25 to 30 Å is sufficient to provide the measured EOT impedance. This finding is critical in that impedance degradation between neutralizer common and keeper is purely a facility effect and would not occur if the engine were operated in the vacuum of space.

Neutralizer keeper-to-ground impedance reduced dramatically during the first 2000 h of operation and was 40 kΩ at the conclusion of the test. Inspection of the electrical path from the ground connection to the keeper electrode also indicated the presence of a carbon coating, providing a path from the keeper to the tank-grounded inner cylinder. The thickness of the coating has yet to be ascertained. In addition to the carbon path from keeper to ground, what appears to be melted braze material in the vicinity of the keeper wire termination was found between the concentric keeper and grounded cylinders. The extent of this redeposited braze has not yet been ascertained, but it could potentially have contributed to the conductive path across the ceramic and hence the 40 kΩ impedance at the end of the test. It is unknown at this time if this apparent flow of braze material beyond the nominal location was a part of the nominal manufacturing process.

3. *Insert Analysis*

SEM and EDX analysis of the fracture surface of the neutralizer insert was also performed. Figure 24 is a comparison of the Ba/W ratio for the unoperated insert and neutralizer insert at the downstream end as a function of depth from the surface. Like the cathode insert, the neutralizer insert surface was also depleted of impregnate material relative to the unoperated insert. Impregnate material was found roughly 300 μm from the surface, with a signal strength similar to that of the unoperated insert. Similar to the discharge cathode insert condition, the absence of oxide layers on the insert surface and limited impregnate depletion suggests that the

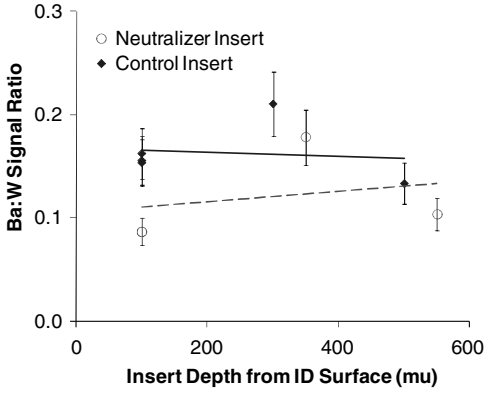

Fig. 24 Ba/W ratio comparison of a 30,000 h neutralizer cathode insert with an unoperated insert as a function of depth from the ID surface.

neutralizer insert was healthy and fully functional as an electron emitter. Tungsten deposition, however, was significantly less than that observed on the discharge cathode insert and cathode orifice plate. The comparatively lower tungsten deposition is thought to be consistent with the lower current operation and, therefore, temperature of the neutralizer insert.

E. Ion-Optics Performance and Wear

1. In-Test Performance

Wear of the ion-optics system during the test was characterized from perveance electron backstreaming and screen-grid transparency measurements taken at the nominal operating point and periodically over the entire throttling range [9]. These measurements indicated the ability of the system to extract, focus, and accelerate ionized propellant to produce thrust. They also provided insight into the geometry or erosion of the accelerator-grid apertures and changes to the intragrid electric field.

Accelerator-grid erosion plays a key role in understanding the performance of the ion-optics system. The physical mechanism responsible for erosion is the production of charge-exchange ions in the intragrid region and downstream of the accelerator grid. The charge-exchange ions produced in the intragrid region bombard and erode the accelerator-grid apertures, whereas the charge-exchange ions produced downstream are responsible for the characteristic pits and groove erosion on the downstream grid webbing [17]. Charge-exchange-ion production is proportional to the neutral density; therefore, the higher density in a vacuum chamber, as compared with the space environment, may aggravate erosion during ground testing. Accelerator-grid aperture enlargement and severe grid-webbing erosion will affect the optics system's ability to focus the individual beamlets (perveance limit) and prevent beam-neutralizing electrons from entering the discharge chamber (electron backstreaming limit). Variations and rate trends in the perveance and electron backstreaming limits, which were monitored on a weekly basis, provided further insight into the accelerator-grid erosion process. The trends in both perveance and electron backstreaming, discussed in great detail in [7–9], correspond to the increase in accelerator aperture diameter with thruster wear. In addition, accelerator-grid erosion was found to be most severe at the high power levels and negligible at the minimum-power point. TH15 operation yielded the highest rates of aperture enlargement, electron backstreaming, and perveance limit variation, corresponding to the higher beam-current density and beam voltage of TH15 (2.3 kW), as compared with TH0 (0.5 kW) operation.

Although accelerator-grid aperture enlargement, including chamfering of the downstream end of the apertures, can account for much of the changes to the optics performance during the course of the test, the final TH15 segment exhibited a markedly faster rate of performance degradation in the ion optics than the previous 2.3 kW test segments. It is believed that during the final TH15 segment, the ongoing grid-gap reduction and the resultant increase in the electric field may have also contributed to the observed rapid reduction in optics performance. Specifically, at 29,000 h of operation, electron backstreaming could no longer be prevented at the TH15 operating point. This finding demonstrated that accelerator-grid wear is the critical life-limiting mechanism at full-power operation and was the first failure mode exhibited by FT2 [7]. Although the engine could not be operated at TH15 (2.3 kW) at nominal levels from 29,000 h to the conclusion of the test, it was still fully operational from TH0 to TH12. The grid-gap change will be discussed in more detail in following sections.

2. Posttest Inspection

Posttest measurements of the ion-optics assembly included measurement of the cold grid gap, individual grid aperture diameters, grid thickness, grid curvature, dish depth, upstream and downstream erosion profiles with a laser profilometer, and inspection with the SEM. Analytical and computational analysis [17] is also associated with the posttest analysis, including a finite element model analysis of the stresses experienced by the grids during operation. A more detailed quantitative analysis of the ion-optics wear and posttest condition, as well as measurement techniques used, can be found in [18].

Optical inspection of the accelerator grid revealed that pits in the center of the grid webbing, out to approximately 6.6 cm (2.6 in.) radially, went through the entire accelerator-grid thickness (Figs. 25 and 26). Laser-profilometry data of the downstream accelerator grid indicated that up to 40% of the grid thickness was removed in the groove regions in the grid webbing at the center (Fig. 27). It should be noted that contour variations in the empty space inside of the apertures are from light reflections with the granite table on which the sample was inspected. The profilometry data were also used to determine mass loss per aperture due to erosion of the grid webbing and aperture walls. Analysis of the pits and grooves data indicates a mass loss per aperture of $\sim$3.5 mg/aperture near the center of the grid decreasing to about 2.8 mg/aperture at about 8.6 cm from the center of the grid. The grid transitions from net erosion to net carbon deposition between about 8.6 and 9.5 cm. The mass-loss data were integrated over the entire grid, yielding an estimate of 18.3 *g* mass loss in the pits and grooves. Preliminary mass-loss estimates from aperture enlargement integrated over the entire grid indicate a total of 12.2 *g* lost due to aperture-wall erosion. The net calculated mass loss (which includes aperture-wall loss, grid-webbing erosion, and net deposition of carbon) indicates a total mass loss of 30.2 *g* for the accelerator grid.

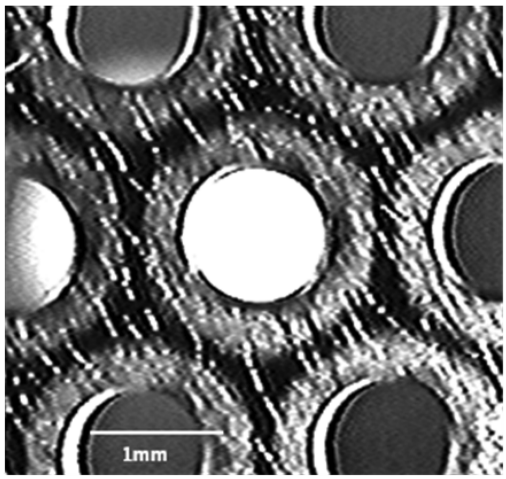

Fig. 25 Image of the downstream side at the center of the accelerator grid after 125 h of operation as taken by the in-tank video system. The beginnings of erosion can be seen in the interaperture spacing.

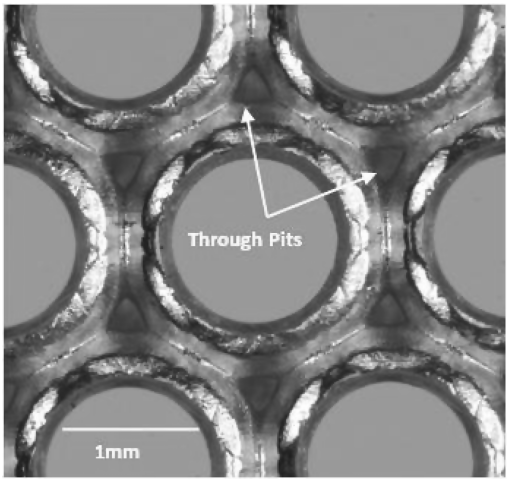

Fig. 26 Image of the downstream side at the center of the accelerator grid after 30,352 h of operation. Significant aperture enlargement, grooves, and pits are evident.

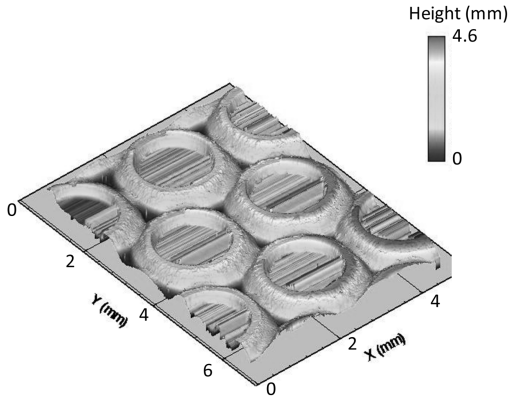

Fig. 27 Three-dimensional view of posttest profilometry scans from the center region of the accelerator grid. The scans captures the pits, grooves, and aperture enlargement and texturing of the downstream surface.

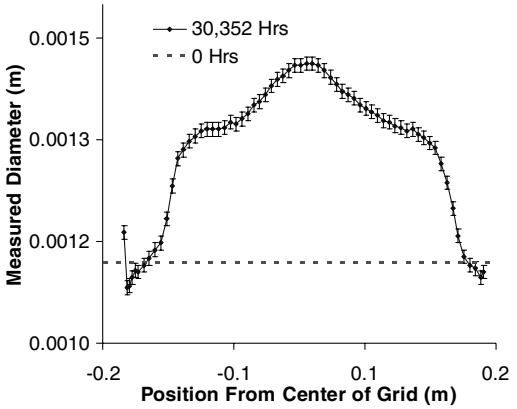

Fig. 28 Comparison of accelerator-grid minimum aperture diameter as a function of position from the center at the beginning of the test and after 30,352 h.

Optical inspection and laser-profilometer scans of the screen grid at different radial locations revealed no measurable aperture enlargement; however, measurable chamfering of the upstream webbing occurred. It is estimated that at the center aperture the mass loss was 0.96 mg/aperture or 17% of the initial mass of webbing surrounding the aperture. Preliminary estimates indicate that 3.2 *g* of material were lost from the screen grid due to upstream chamfering.

Posttest mass measurements of the screen and accelerator-grid assembly made with a high-precision balance concur with the profilometry calculations to within 2 and 10%, respectively, thereby validating the profilometry mapping technique and subsequent data analysis performed [18].

Although the laser-profilometer data provide an excellent three-dimensional erosion profile over the grid surface, physical measurements accurately defining the maxima and minima of key parameters must be made. Therefore, SEM micrographs were used to provide accurate measurements of grid thickness, thickness of thin-film deposits, extent of erosion, and chamfering of the aperture walls. Details on these measurements can be found in [18,19].

Optical measurements of the accelerator- and screen-grid aperture diameters were made using precision dowels and an optical coordinate-measuring machine (CMM). A complete two-dimensional mapping of the accelerator-grid minimum aperture diameters was also performed (Figs. 28 and 29). These measurements document the smallest diameter of each aperture and do not measure chamfering of the walls. Laser profilometry was used to measure the erosion profile of the aperture walls and will be discussed later. The measurements indicate that the accelerator-grid minimum aperture diameters increased from pretest values by up to 25% in the center of the grid, as compared with 20% for the LDT, which operated exclusively at TH15 for only 8000 h [3]. This was less enlargement than predicted, but laser-profilometry data indicate that the accelerator-grid apertures were significantly chamfered at the downstream end by 30,352 h of operation. This differs from the LDT, in which the cusps had been eroded away, leaving cylindrical apertures with no downstream chamfering [3].

The two-dimensional mapping indicates that the peak aperture enlargement occurred slightly off of the thruster centerline, which is spatially consistent with the peak current density obtained during the ELT with a Faraday probe [7,19]. Measurements of screen-grid aperture diameters indicate that they were unchanged from pretest values over the entire grid surface. However, laser-profilometer data indicate the presence of chamfers eroded into the upstream side of screen-grid webbing. The upstream screen-grid erosion is due to discharge chamber ions striking and eroding the grids. The current striking the screen grid is proportional to the beam-current-density profile, which is peaked on axis. Both double and single ions cause the erosion with the erosion due to doubles dominating because they have twice the kinetic energy of the singles. The NSTAR engine has a double-to-single current ratio of 0.15 to 0.2, which results in a sputter rate 3.5 to 4.2 times higher than if all the ions were singly ionized [8,20]. Physical measurements of the screen and accelerator-grid

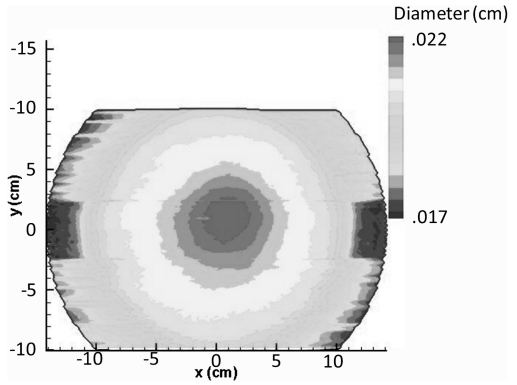

Fig. 29 Contour plot of accelerator-grid aperture diameters indicating radial dependence over the grid.

thickness indicate the absence of change from the pretest thickness in regions without erosion.

The posttest measurement of the ion-optics-assembly cold grid gap indicates a 31% reduction from the initial pretest measurement (Fig. 30). The grid gap was measured with an optical CMM and gap gauges in regions that were physically accessible. Inspection of the disassembled grid set revealed that the accelerator-grid assembly was no longer flat. The accelerator-grid assembly consists of the grid riveted to a molybdenum stiffening ring for structural support [18]. During the posttest disassembly and inspection, it was observed that the tabs of the stiffening ring deformed such that they were in excess of 0.51 mm positive of the nominal downstream grid-plane surface. When reassembly of the optics assembly was attempted, the grids contacted in a nontorqued down condition. All other measurements

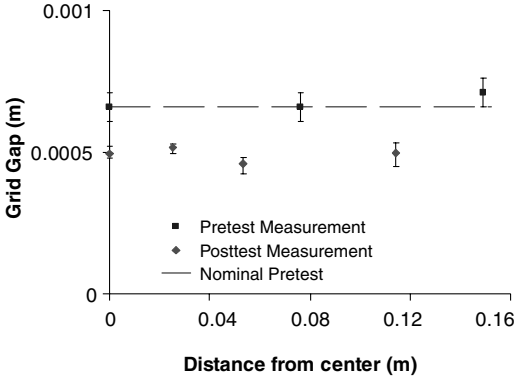

Fig. 30 Comparison of BOL, EOT (30,352 h), and design-specification-normalized grid gap.

of the grid assembly were within the pretest nominal specifications. Therefore, the reduction in grid gap observed at the conclusion of the test was due to the deformation of the accelerator-grid assembly. To determine the cause of the observed posttest deformation, it was necessary to separate the stiffening rings from the grids to determine if the measured tab-height variation was due to a permanent deformation of the stiffening ring or a nonflat grid-mounting surface. Measurements indicate that the stiffening ring exhibited a permanent deformation of 0.051 ± 0.0025 mm from the inside edge to the tab extremity, which is within the design specification, and less than the previously measured 0.51 mm variation when it was riveted to the assembly. Flatness measurements of the accelerator-grid flat region, however, exhibited a deformation of up to 0.211 mm from the inside to outside edge. As the stiffening ring tabs extend roughly 5.1 mm beyond the grid flat, and assuming the deformation is linear, the result is the measured posttest assembled deformation. Therefore, the deformation of the grid-flat region was responsible for the posttest condition of the accelerator-grid assembly, including the grid-gap reduction and rapid reduction in electron backstreaming limit at the conclusion of the test.

It is likely that if the accelerator grid is torqued down to the mounting ring, the mounting tabs flex back, which tend to bow out the grid, thereby reestablishing the measured posttest grid gap. It is theorized that insufficient stress relieving of the accelerator grid is responsible for the permanent deformation. Results of a finite element model of the NSTAR ELT grid set indicate that the stress-relieving of the accelerator-grid assembly during operation at temperature can provide adequate stress to account for the observed accelerator-grid-assembly deformation.

V. Conclusions

A total of 30,352 h of operation and 235 kg of xenon propellant were processed during the ELT before its voluntary termination. Just before the conclusion of the test, the thruster continued to perform well with minimal degradation in thrust, specific impulse, or thrust-vector location for operation between 0.5 and 1.96 kW. Although the accelerator-grid downstream wear was significant, preventing operation at the full-power point, the engine was still fully operational at the mid to lower end of the throttle envelope. Significant discharge cathode keeper erosion continued through to the end of the test, fully exposing the cathode heater and orifice plate. In spite of this, ignition and discharge characteristics remain unchanged and stable when compared with data taken at the beginning of the test. The neutralizer continued to perform nominally through the end of the final TH5 test segment, with no loss of flow rate margin from plume mode or evidence of deposit formation within the orifice.

Examination of the engine components indicate that cathode orifice plate erosion, due to exposure to the discharge plasma, was more severe than previously thought, having eroded through the nominal electron beam weld location. Other notable findings included healthy emitter surfaces for both the discharge and neutralizer inserts and deformation of the accelerator-grid assembly, resulting in a 31% reduction in grid gap.

Acknowledgments

The research described in this paper was carried out at the Jet Propulsion Laboratory, California Institute of Technology, under a contract with NASA. Funding was provided by the In-Space Propulsion Program, managed by NASA Headquarters, Office of Space Science. The authors would like to acknowledge the invaluable efforts of the many people who contributed to the successful completion of the extended-life test and posttest analysis activity. They include Norm Hill of Georgia Institute of Technology; Wayne Ohlinger of Bettis Labs; Al Owens, Keith Goodfellow, James Kulleck, Ron Ruiz, James Polk, Lois Lewis, Ray Swindlehurst, and Bob Brown of the Jet Propulsion Laboratory; Jim Sovey and Mike Patterson of NASA John H. Glenn Research Center at Lewis Field; and Randy Bagget of NASA Marshall Space Flight Center.

References

[1] Polk, J. E., Kakuda, R. Y., Brinza, D., Katz, I., Anderson, J. R., Brophy, J. R., Rawlin, V. K., Patterson, M. J., Sovey, J., and Hamley, J., "Demonstration of the NSTAR Ion Propulsion System on the Deep Space One Mission," International Electric Propulsion Conference Paper IEPC-01-075, Oct. 2001.

[2] Brophy, J. R., Kakuda, R. Y., Polk, J. E., Anderson, J. R., Marcucci, M. G., Brinza, D., Henry, M. D., Fujii, K. K., Mantha, K. R., and Stocky, J. F., "Ion Propulsion System (NSTAR) DS1 Technology Validation Report," Jet Propulsion Lab., California Inst. of Technology Rept. 00-10, Oct. 2000.

[3] Polk, J. E., Anderson, J., Brophy, J., Rawlin, V., Patterson, M., Sovey, J., and Hamley, J., "An Overview of the Results from an 8200 h Wear Test of the NSTAR Ion Thruster," AIAA Paper 99-2446, June 1999.

[4] Polk, J. E., Patterson, M., Brophy, J., Rawlin, V., Sovey, J., Myers, R., Blandino, J., Goodfellow, K., and Garner, C., "A 1000-hour Wear Test of the NASA NSTAR Ion Thruster," AIAA Paper 96-2717, July 1996.

[5] Polk, J. E., and Sovey, J., "The Effect of Engine Wear on Performance in the NSTAR 8000 h Ion Engine Endurance Test," AIAA Paper 97-3387, July 1997.

[6] Christensen, J., "Design and fabrication of a Flight Model 2.3 kW Ion Thruster for the Deep Space 1 Mission," AIAA Paper 98-3327, July 1998.

[7] Sengupta, A., Brophy, J. R., and Goodfellow, K. D., "Status of the Extended Life Test of the Deep Space 1 Flight Spare Ion Engine After 30,352 h of Operation," AIAA Paper 2003-4558, July 2003.

[8] Sengupta, A., Brophy, J. R., and Goodfellow, K. D., "Performance Characteristics of the Deep Space 1 Flight Spare Ion Thruster Long Duration Test After 21,300 h of Operation," AIAA Paper 2002-3959, July 2002.

[9] Anderson, J. R., et al., "Results of an On-Going Long Duration Ground Test of the DS1 Flight Spare Ion Engine," AIAA Paper 99-2857, June 1999.

[10] Brophy, J. R., Marcucci, M., Gates, J., Garner, C., Nakazono, B., and Ganapathi, G., "Status of the Dawn Ion Propulsion System," AIAA Paper 2004-3433, Jul. 2004.

[11] Brophy, J. R., "NASA's Deep Space 1 Ion Engine," *Review of Scientific Instruments*, Vol. 73, No. 2, Feb. 2002, pp. 1071–1078. doi:10.1063/1.1432470

[12] de Groh, K. K., Banks, B. A., and Karniotis, C. A., "NSTAR Extended Life Test Discharge Chamber Flake Analyses," AIAA Paper 2004-3612, July 2004.

[13] Garner, C. R., Sengupta, A., Kulleck, J., and Lui, T., "An Evaluation of the Discharge Chamber of the 30,000 h Life Test of the Deep Space 1 Flight Spare Ion Engine," AIAA Paper 2004-3609, July 2004.

[14] Sengupta, A., "Destructive Physical Analysis of Hollow Cathodes from the Deep Space 1 Flight Spare Ion Engine 30,000 h Life Test," International Electric Propulsion Conference Paper 2005-026, Oct. 2005.

[15] Sarver-Vehey, T. R., and Soulas, G. C., "Destructive Evaluation of a Xenon Hollow Cathode After a 28,000 h Life Test," AIAA/ASME/SAE/ASEE Joint Propulsion Conference and Exhibit, 34th, AIAA Paper 1998-3483, Cleveland, OH, 1998.

[16] Brophy, J. R., Brinza, D. E., Polk, J. E., Henry, M. D., and Sengupta, A., "The DS1 Hyper-Extended Mission," 2002 Joint Propulsion Conference, AIAA Paper 2002-3673, Indianapolis, IN, July 2002.

[17] Anderson, J. R., Katz, I., and Goebel, D., "Numerical Simulation of Two-Grid Ion Optics Using a 3D Code," 40th AIAA/ASME/SAE/ASEE Joint Propulsion Conference and Exhibit, AIAA Paper 2004-3782, Fort Lauderdale, FL, July 2004.

[18] Anderson, J. R., Sengupta, A., Brophy, J. R., "Post-Test Analysis of the Deep Space 1 Spare Flight Thruster Ion Optics," AIAA Paper 2004-3610, July 2004.

[19] Sengupta, A., Anderson, J., Brophy, J., Garner, C., Kulleck, J., de Groh, K., and Banks, B., "The 30,000 h Life Test of the DS1 Flight Spare Ion Thruster, Final Report," NASA TP 2004-213391, 2004.

[20] Doerner, R., Whyte, D. G., and Goebel, D. M., "Sputtering Yield Measurements During Low Energy Xenon Plasma Bombardment," *Journal of Applied Physics*, Vol. 93, No. 9, May 2003, pp. 5816–5823. doi:10.1063/1.1566474

R. Myers
Associate Editor